J. Fluid Mech. (2024), *vol*. 983, A45, doi:10.1017/jfm.2024.168

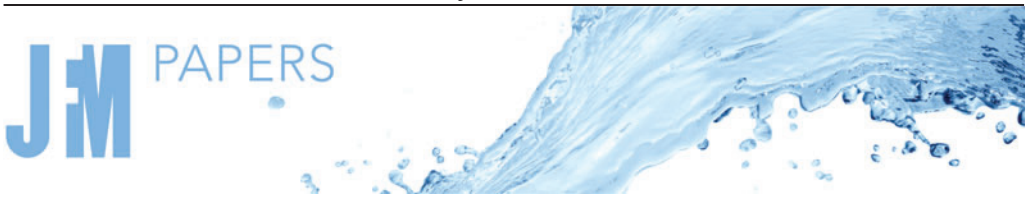

Segregation–rheology feedback in bidisperse granular flows: a coupled Stokes' problem

Tomás Trewhela†

Facultad de Ingeniería y Ciencias, Universidad Adolfo Ibañez, Av. Padre Hurtado 750, 2562340 Viña del Mar, Chile

(Received 25 August 2023; revised 11 February 2024; accepted 16 February 2024)

The feedback between particle-size segregation and rheology in bidisperse granular flows is studied using the Stokes' problem configuration. A method of lines scheme is implemented to solve the coupled momentum and segregation equations for a normally graded particle size distributed bulk at constant solids volume fraction. The velocity profiles develop quickly into a transient state, decoupled from segregation yet determined by the particle size. From this transient state, the velocity profile changes due to the particles' relative movement, which redistributes the frictional response, hence its rheology. Additionally, the particles' relative friction is modified via a frictional coefficient ratio, by analogy with the particles' size ratio. While positive values of this coefficient exacerbate the nonlinearity of the velocity profiles induced by size differences, negative values dampen this behaviour. The numerical solutions reproduce well the analytical solutions for the velocity profile, which can be obtained from the steady-state conditions of the momentum and segregation equations for the transient and steady states, respectively. Segregation–momentum balances and four characteristic time scales can be established to propose two non-dimensional quantities, including specific Schmidt and Péclet numbers that describe broadly the segregation–rheology feedback. The proposed scheme, theoretical solutions and non-dimensional numbers offer a combined approach to understand segregation and flow dynamics within a granular bulk, extensible across many flow configurations.

Key words: granular materials, particle/fluid flow

1. Introduction

Size segregation is responsible for important mobility feedback in granular flows (Barker *et al.* 2017; Gray 2018; Umbanhowar, Lueptow & Ottino 2019; Edwards *et al.* 2023). Since particle size d is a defining parameter for most rheological models of dry granular

† Email address for correspondence: tomas.trewhela@uai.cl

materials (GDR-MiDi 2004; Jop, Forterre & Pouliquen 2006; Kamrin & Koval 2012; Henann & Kamrin 2013; Kim & Kamrin 2020), segregation-induced grain movement alters the very same mechanical response that generates segregation in the first place. Such feedback determines the flow's runout, the formation of levees, fingers, and blunt or bulbous fronts in debris flows, all tied to coarse grains segregating towards the flow's free surface (Woodhouse *et al.* 2012; Denissen *et al.* 2019; Edwards *et al.* 2023).

Numerical simulations and experiments have been pivotal to shed light on the rich segregation–rheology coupling in granular flows. Recent experiments in two- and three-dimensional shear boxes unravelled a scaling law for bidisperse particle-size segregation; asymmetric segregation fluxes depend on shear rate $\dot{\gamma}$, particle sizes, their size ratio R_d and pressure p (i.e. the inertial number I, implicitly), and local particle concentrations (Trewhela, Ancey & Gray 2021*a*; Trewhela, Gray & Ancey 2021*b*). These experimental results are consistent with previous observations on pressure-dependent segregation (Golick & Daniels 2009) and the intrinsic asymmetric nature of segregation fluxes (van der Vaart *et al.* 2015; Jones *et al.* 2018). Similar results, in terms of an inertial number I dependence, were obtained in discrete element method simulations, by modelling a bedload transport flow (Chassagne *et al.* 2020) and a shear flow (Bancroft & Johnson 2021). Based on the empirical scaling law of Trewhela *et al.* (2021*a*), Barker *et al.* (2017) performed simulations of fully coupled granular flows down a slope and in a square rotating drum. They discussed the intricate segregation–rheology feedback, concluding that it is not clear how subtle changes in flow properties influenced the coupling mechanisms and their impact on the flows' overall dynamics.

In 1850, G.G. Stokes proposed a problem concerning a semi-infinite layer of fluid in contact with a horizontal and infinitely long plate. The plate suddenly slides horizontally at $t = 0$ with finite speed, therefore transferring shear to the fluid (Stokes 1850). This problem, known as Stokes' first problem (or Rayleigh's problem), offers an idealized, yet practical configuration for the study of sheared flows (Rayleigh 1911). Besides the historical and theoretical interest that this problem has had for fluid mechanics (Stewartson 1951; Tokuda 1968; Preziosi & Joseph 1987; Jordan & Puri 2005; Jerome & Di Pierro 2018), its flow configuration has various applications for experimental and industrial facilities using granular materials, e.g. shear cells or conveyor belts (Golick & Daniels 2009; van der Vaart *et al.* 2018; Trewhela & Ancey 2021). Using the $\mu(I)$-rheology (GDR-MiDi 2004; Jop *et al.* 2006), Jerome & Di Pierro (2018) studied Stokes' problem for granular flows, developing numerical and analytical solutions for momentum transfer and velocity profiles within a semi-infinite granular medium. Their analysis focused on a sheared layer h, which developed when applying shear τ_w at the upper boundary, and depended on a kinematic granular viscosity $\nu_g \sim d$, an observation also recovered with kinetic theory in gravitational granular currents (e.g. Larcher & Jenkins 2019) and discrete element method simulations (Jing *et al.* 2022). Intuitively, changes in particle-size distribution and subsequent segregation will significantly alter momentum diffusion within the bulk, so coupling this process with segregation is not straightforward.

This work investigates the segregation–rheology feedback, its coupling and impact on the overall dynamics of dense granular flows. Stokes' first problem configuration, with the theoretical and numerical framework for the segregation–rheology feedback, is introduced in § 2. The numerical and steady-state solutions are presented in § 3, where emphasis is put on the crucial role of size ratio and frictional coefficient differences in the flow dynamics. Analytical solutions and characteristic time scales are sought, so that non-dimensional numbers are proposed to describe the segregation–rheology feedback. The conclusions in

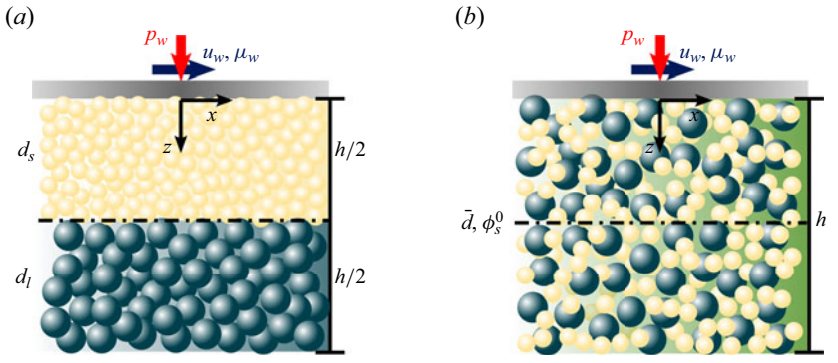

Figure 1. Stokes' problem for a dense bidisperse granular flow: an infinite plate shears a granular bulk made of small ($\nu = s$) and large ($\nu = l$) particles (each particle species is characterized by its diameter d_ν and partial volume concentration ϕ_ν). The plate suddenly moves with constant velocity u_w at $t = 0$, imposing pressure p_w with a frictional coefficient μ_w at contact with the granular media. (*a*) An inversely graded initial condition (segregated, but unstable) for the granular bulk, with partial concentrations $\phi_s = 1$ on top and $\phi_s = 0$ ($\phi_l = 1 - \phi_s = 1$) at the bottom. (*b*) Initially mixed granular bulk (unstable) condition, with uniform small particle concentration ϕ_s^0 and an equivalent concentration-averaged diameter $\bar{d} = \phi_s d_s + \phi_l d_l$ through the bulk's sheared layer h.

§ 4 put focus on the found numerical and analytical solutions, the description provided by the non-dimensional balances and their applicability in general flow configurations.

2. Governing equations and numerical solutions

2.1. *Stokes' problem for a dense bidisperse granular flow*

Consider a semi-infinite granular material formed by a dense bidisperse mixture of grains that share the same density ρ_* but differ in size (figure 1). The particle sizes d_s and $d_l > d_s$ define grain species $\nu = \{s, l\}$ of small and large particles, respectively. The contribution of each species to the solids volume fraction Φ is set by its partial volume concentration ϕ_ν per unit volume of grains, so that $\phi_s + \phi_l = 1$. A plate of infinite length lies initially at rest over the bulk and is set to slide horizontally with velocity u_w at $t = 0$, and a frictional coefficient μ_w. Under these conditions and at constant Φ, such that $\rho = \Phi\rho_*$, the mass and momentum conservation equations for the whole granular material (small and large particles) in the x–z directions reduce to

$$\frac{\partial u}{\partial x} = 0, \quad \rho_* \Phi \frac{\partial u}{\partial t} = -\frac{\partial \tau_{xz}}{\partial z}, \quad \frac{\partial p}{\partial z} = \rho_* \Phi g, \tag{2.1a–c}$$

where g is the gravitational acceleration in the z-direction, u is the component of the velocity field $\boldsymbol{u}$ in the x-direction, and τ_{xz} is the x–z component of the deviatoric shear stress tensor $\boldsymbol{\tau}$. In dense granular flows, pressure p and shear stress τ relate through a Coulombic frictional coefficient μ so that $\tau = \mu p$. From (2.1*c*), pressure $p = p_w + \rho_* g z$ can be considered lithostatic with p_w imposed at the plate above. For various flow configurations, GDR-MiDi (2004) showed that μ depends on the dimensionless inertial number $I = \dot{\gamma} d/\sqrt{p/\rho_*}$, with d the particle diameter and $\dot{\gamma} = 2\,\|\boldsymbol{D}\| = |\mathrm{d}u/\mathrm{d}z|$ the shear rate. Barker & Gray (2017) introduced a partial regularization for the $\mu(I)$-rheology (Jop *et al.* 2006), so that its well-posedness range could be extended. This regularization can be

$$\rho_* = 2500\ \text{kg m}^{-3}, \quad \Phi = 0.6, \quad \mu_1 = 0.342, \quad \mu_2 = 0.557, \quad I_0 = 0.069,$$
$$\mu_\infty = 0.05, \quad \alpha = 1.9, \quad I_1 = 0.005, \quad A = 1.5647 \times 10^4$$

Table 1. Intrinsic density ρ_*, solids volume fraction Φ, and frictional parameters μ_1, μ_2 and I_0 for the $\mu(I)$-rheology (Jop *et al.* 2006). Frictional coefficient μ_∞ with the parameters α, I_1 and A (computed) for the partial regularization of the $\mu(I)$-rheology were proposed and measured by Barker & Gray (2017) for $d_l = 143$ μm glass beads.

introduced by considering the extended function

$$\mu(I) = \begin{cases} \sqrt{\alpha / \log(A/I)}, & \text{for } I \leq I_1, \\ \dfrac{\mu_1 I_0 + \mu_2 I + \mu_\infty I^2}{I + I_0}, & \text{for } I > I_1, \end{cases} \tag{2.2}$$

where μ_1 is the static friction coefficient, μ_2 is the dynamic friction coefficient, and I_0 are the original parameters employed by Jop *et al.* (2006), corresponding to particle-dependent or material constants. The remaining parameters μ_∞, I_1 and α are also material-dependent and were introduced by Barker & Gray (2017). While μ_∞ holds physical meaning in the context of rapid granular flows beyond μ_2 (Holyoake & McElwaine 2012; Barker & Gray 2017), α and I_1 are just mathematical fitting constants. Finally, A is a constant that guarantees continuity of the regularized function and is calculated using the latter parameters. All the frictional coefficients and material constants used for this work follow those in Barker *et al.* (2017) and are detailed in table 1.

The bidisperse nature of the considered granular material can be included via (i) a concentration-averaged diameter $\bar{d}$ in I (Tripathi & Khakhar 2011; Chassagne *et al.* 2020; Bancroft & Johnson 2021), and (ii) a concentration-averaged frictional coefficient $\bar{\mu}$ in (2.2). Similarly to the concentration-averaged diameter $\bar{d} = \phi_s d_s + \phi_l d_l$ (Rognon *et al.* 2007; Tripathi & Khakhar 2011), a concentration-averaged $\bar{\mu}$ definition can be proposed in the form $\bar{\mu} = \mu_s \phi_s + \mu_l \phi_l$, where μ_ν is the frictional coefficient for the ν species. Arranging the terms, this $\bar{\mu}$ definition can be expressed as a function of the ratio between the species' frictional coefficients $R_\mu = \mu_l / \mu_s$, resulting in

$$\bar{\mu} = (1 - \chi_\mu \phi_s) R_\mu \mu_s, \tag{2.3}$$

which prompts the definition $\chi_\mu = (R_\mu - 1)/R_\mu \in (-\infty, 1]$. This expression assumes that I_0 is invariant with size, and only the frictional coefficients μ_i $(i = \{1, 2, \infty\})$ in table 1 are size-dependent.

As expected, the inclusion of the $\mu(I)$-rheology poses several difficulties for numerical schemes, particularly when the bulk is at rest or in steady state (Cawthorn 2011; Barker & Gray 2017; Jerome & Di Pierro 2018). To overcome this issue, the analysis can be focused on a sheared layer h, defined as

$$h = \left(\frac{\mu_w}{\mu_1} - 1 \right) \frac{p_w}{\rho g \Phi}, \tag{2.4}$$

where μ_w and p_w are the frictional coefficient and pressure applied at the upper plate, respectively. This shear layer h definition was already employed in the solution of the monodisperse granular Stokes' problem, but still poses difficulties for numerical schemes and solutions (Cawthorn 2011; Jerome & Di Pierro 2018).

2.2. *Bidisperse particle-size segregation*

Particle-size segregation in sheared dense granular flows is driven primarily by gravity and friction. This gravity-driven segregation is the result of two mechanisms: small particles fall through gaps via kinetic sieving (Middleton 1970), and large particles are squeezed by surrounding particles, expulsed from their position (Savage & Lun 1988). There are, however, other segregation mechanisms, many of which appear in different configurations and can be described employing kinetic theory and quantities such as granular temperature (e.g. Larcher & Jenkins 2019; Neveu *et al.* 2022). In this work however, segregation mechanisms are not discussed, and focus is put on the shear and gravity-driven particle-size segregation problem for dense granular flows under a frictional regime (Ancey & Evesque 2000; GDR-MiDi 2004). The segregation dynamics to be studied with the Stokes' problem is well described by the mentioned shear-driven mechanisms and well documented in theoretical, numerical and experimental work (e.g. May *et al.* 2010; van der Vaart *et al.* 2015; Guillard, Forterre & Pouliquen 2016; Trewhela & Ancey 2021; Edwards *et al.* 2023), and has a determinant role for various geophysical granular flows (Delannay *et al.* 2017; Gray 2018).

For the Stokes' problem in figure 1(*a*), the bidisperse segregation equations for ϕ_s and ϕ_l are

$$\frac{\partial \phi_s}{\partial t} + \boldsymbol{\nabla}\cdot\left(f_{sl}\phi_s\phi_l\,\frac{\boldsymbol{g}}{|\boldsymbol{g}|}\right) = \boldsymbol{\nabla}\cdot(\mathcal{D}_{sl}\,\boldsymbol{\nabla}\phi_s), \quad \frac{\partial \phi_l}{\partial t} - \boldsymbol{\nabla}\cdot\left(f_{sl}\phi_s\phi_l\,\frac{\boldsymbol{g}}{|\boldsymbol{g}|}\right) = \boldsymbol{\nabla}\cdot(\mathcal{D}_{sl}\,\boldsymbol{\nabla}\phi_l), \tag{2.5a,b}$$

where f_{sl} is the segregation velocity magnitude, and $\mathcal{D}_{sl} = \mathcal{A}\dot{\gamma}\bar{d}^2$ is the particles' diffusivity, with $\mathcal{A} = 0.108$ and $\bar{d}$ a mean diameter (Utter & Behringer 2004). Note that the inclusion of the gravitational acceleration considers the fact that segregation in dense granular flows is a shear and gravity-driven process due mainly to the kinetic sieving mechanism (Middleton 1970). Recently, Trewhela *et al.* (2021*a*) presented an experimentally based scaling law for f_{sl}, obtaining

$$f_{sl} = \left(\frac{\hat{\rho}\hat{\mathcal{B}}\rho_* g\dot{\gamma}\bar{d}^2}{\mathcal{C}\rho_* g\bar{d} + p}\right)[(R_d - 1) + \mathcal{E}(1-\phi_s)(R_d-1)^2], \tag{2.6}$$

where $R_d = d_l/d_s$ is the particles' size ratio, and $\hat{\rho} = (\rho_* - \rho_*^f)/\rho_*$ is the relative density difference between grains and interstitial fluid of density ρ_*^f. The constants $\hat{\mathcal{B}} = \mathcal{B}/\hat{\rho} \approx 0.713$, $\mathcal{C} = 0.271$, $\mathcal{E} = 2.096$ were obtained from a least squares fit of their experimental data (Trewhela *et al.* 2021*a*). The concentration-averaged particle diameter $\bar{d}$ gives the segregation velocity f_{sl} its asymmetric behaviour (van der Vaart *et al.* 2015), since after rearranging and introducing the size ratio R_d in its definition,

$$\bar{d} = (1 - \chi_d\phi_s)d_l, \tag{2.7}$$

where $\chi_d = (R_d - 1)/R_d \in [0, 1]$ is the asymmetry parameter that shifts the maximum segregation velocities for small and large particles (Gray 2018). The definition for $\bar{d}$ is replaced in (2.6) to obtain

$$f_{sl} = \left(\frac{\rho_* g\mathcal{B}\dot{\gamma}(R_d - 1)}{p_w + \rho_*\Phi gz}\right)[1 + \mathcal{E}(1-\phi_s)(R_d-1)](1-\chi_d\phi_s)^2 d_l^2, \tag{2.8}$$

where $p = p_w + \rho_*\Phi gz$ replaced the pressure p in (2.6). The term $\mathcal{C}\rho_* g\bar{d}$ was replaced by p_w, since it was introduced by Trewhela *et al.* (2021*a*) to avoid numerical singularities when $p = 0$ at the free surface, a purpose that p_w serves as well by definition.

From these definitions, the theoretical appearance of the segregation–rheology feedback is clear. The shear rate $\dot{\gamma}$ and pressure p are decisive for the segregation velocity f_{sl} magnitude, and reciprocally, the particle concentrations ϕ_v determine the frictional coefficient μ, explicitly and implicitly via the averaged frictional coefficient $\bar{\mu}$ and the inertial number I, respectively (Golick & Daniels 2009; Chassagne *et al.* 2020; Bancroft & Johnson 2021; Trewhela *et al.* 2021*a*).

2.3. *Non-dimensional coupled system of equations*

Equation (2.8) synthesizes the interdependence between flow and particle distribution, hence a rheology and particle-size segregation feedback. By replacing the definitions made in §§ 2.1 and 2.2, and introducing the non-dimensional variables $\hat{t} = u_w t/h$, $\hat{z} = z/h$, $\hat{u} = u/u_w$, $\hat{p} = p/p_w$, $\hat{f}_{sl} = f_{sl}/u_w$ and $\hat{\mathcal{D}} = \mathcal{D}_{sl}/(hu_w)$ into (2.1*a–c*) and (2.5*a*,*b*), the coupled partial differential equation (PDE) system for $\hat{u}$ and ϕ_s, hence for $\phi_l = 1 - \phi_s$, can be obtained:

$$\frac{\partial \hat{u}}{\partial \hat{t}} + \frac{\partial}{\partial \hat{z}}\left((1 - \chi_\mu \phi_s) R_\mu \mu_s \hat{p}\right) = 0, \quad \frac{\partial \phi_s}{\partial \hat{t}} + \frac{\partial}{\partial \hat{z}}\left(\hat{f}_{sl}\phi_s(1-\phi_s) - \hat{\mathcal{D}}\,\frac{\partial \phi_s}{\partial \hat{z}}\right) = 0, \tag{2.9a,b}$$

where the coupling with the velocity $\hat{u}$ in (2.9*a*) comes from the non-dimensional segregation velocity $\hat{f}_{sl}$ (see (2.8)) and particle diffusivity $\hat{\mathcal{D}}$, which are both shear rate $\dot{\gamma}$-dependent (Utter & Behringer 2004; Trewhela *et al.* 2021*a*). A non-dimensional segregation equation for ϕ_l is not included in the PDE system due to ϕ_l being the reciprocal of $\phi_s = 1 - \phi_l$. Because of their nonlinear nature, (2.9*a*,*b*) do not admit analytical solutions, but they can be solved separately numerically for the uncoupled cases (Cawthorn 2011; Jerome & Di Pierro 2018; Trewhela *et al.* 2021*a*).

2.4. *Numerical method*

The coupled PDE system in (2.9*a*,*b*) is solved using the method of lines (MOL) (Schiesser & Griffiths 2009). Schaeffer *et al.* (2019) used a similar numerical approach as a proof of concept to study compressibility in granular flows. In this work, the robustness of MOL was first tested for the uncoupled segregation equation in (2.5*a*,*b*), as validated by Trewhela *et al.* (2021*a*, figure 13) against the experimental results of van der Vaart *et al.* (2015). Second, the uncoupled monodisperse granular flow equation in (2.9*a*) was solved and compared to the solution presented by Cawthorn (2011, figure 2.10) and Jerome & Di Pierro (2018) (figure 2*a*) for $p_w = 100$ Pa, $u_w = 1$ m s^{-1} and $\mu_w = 0.5$, with the parameters in table 1. The plotted profiles for $\hat{u}$ in figure 2(*b*) also resemble those of Guillard *et al.* (2016, figures 2*c*,*e*), which were obtained using discrete numerical simulations for $g = 0$ and $g = 9.81$ m s^{-2} and for a similar flow configuration. This resemblance validates the presented theoretical framework and numerical scheme.

In this work, a particular pressure $p = p_w$ condition is used for the numerical solutions. A linear pressure (lithostatic) distribution adds further complexity to the numerical scheme with no relevant insights into the segregation–rheology feedback. Velocity profiles $\hat{u}$ for both pressure distributions are compared in figures 2(*b*,*c*) to see the influence of these distributions in the computations. Despite the fact that there are slight differences when comparing the solutions, these are not important compared to the cost of compromising the method's robustness. Pressure is still relevant for segregation (as seen in (2.8) and discussed briefly in Appendix A), but overall segregation dynamics

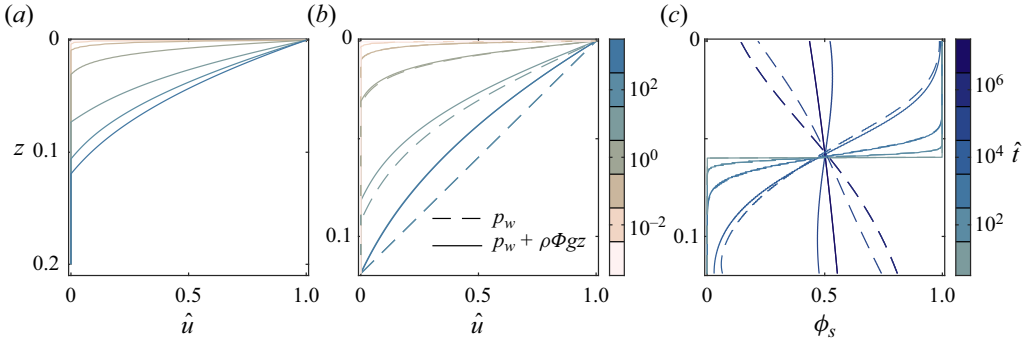

Figure 2. (*a*) Velocity profile $\hat{u}$ solutions (2.9*a*) at different times $\hat{t}$ for the monodisperse case ($\phi_s = 0$) and lithostatic pressure distribution with $p_w = 100$ Pa, $u_w = 1$ m s^{-1} and $\mu_w = 0.5$, similarly to the solutions found by Cawthorn (2011) and Jerome & Di Pierro (2018). (*b*,*c*) Comparison of the velocity profiles $\hat{u}$ and small particle concentration ϕ_s solutions for different times $\hat{t}$ for linear (lithostatic) $p = p_w + \rho g \Phi z$ (continuous line) and constant pressure $p = p_w$ (dashed line) distributions under the same values for the wall parameters u_w, p_w and μ_w with those of (*a*).

does not change substantially when a constant pressure distribution is imposed over the lithostatic distribution. The latter assumption is particularly justified when considering a highly confined granular bulk, in which case $p_w \gg \rho_* g \Phi h$. In contrast, the condition where p_w is neglected in comparison to $\rho_* g \Phi z$ poses difficulties to the numerical schemes since segregation velocity $f_{sl} \to \infty$ as $z \to 0$.

Figures 2(*b*,*c*) give a first glance at the different time scales at which the segregation–rheology feedback operates. A first time scale is that of momentum diffusion within the granular bulk, related to the granular flow rheology, and visible in the fast development of the velocity profile in figure 2(*b*). The other two time scales are longer than the former and are related to particle segregation and diffusion processes. These processes are visible in the slow changes of particle concentration profiles ϕ_s in figure 2(*c*).

3. Results

3.1. *Effect of size ratio in the segregation and velocity profiles*

To demonstrate the crucial role of particle sizes and segregation in the shear flow dynamics, the vertical distributions of small particles ϕ_s and horizontal velocity $\hat{u}$ are computed as functions of time $\hat{t}$ for three particles size ratios $R_d = \{1.25, 2, 3.33\}$, keeping $p_w = 100$ Pa, $\mu_w = 0.5$ and $u_w = 0.2$ m s^{-1} constant (figure 3). The initially unstable arrangement of small particles over large ones influences the velocity $\hat{u}$ profiles; all reach a transient state at $\hat{t} \approx 10^2$, only to be then altered by segregation. From $\hat{t} > 10^2$, the linear velocity profiles $\hat{u}$ for both species, and featuring a slope change at the small–large particle interface, changes into a nonlinear smooth distribution for the final steady-state condition. At initial times, segregation does not influence the velocity profile $\hat{u}$ or the time scale to attain the transient linear state. Therefore, momentum transfer is uncoupled from segregation, with the latter acting at longer time scales, an observation made in various experiments and flow configurations (Golick & Daniels 2009; Tripathi & Khakhar 2011; van der Vaart *et al.* 2015; Trewhela & Ancey 2021). Nonetheless, size ratio R_d influences the transient linear state, determining the velocity vertical gradient, a result also observed by Tripathi & Khakhar (2011) and corroborated by Barker *et al.* (2017).

$$R_d = d_l/d_s = \{1.25, 2, 3.33\}, \quad \chi_d = (R_d - 1)/R_d = \{0.2, 0.5, 0.7\},$$
$$R_\mu = \mu_l/\mu_s, \quad \chi_\mu = (R_\mu - 1)/R_\mu = \{-0.03, -0.02, -0.01, 0, 0.01\},$$
$$p_w = \{100, 300, 1000, 10\,000\}\ \text{Pa}, \quad u_w = \{0.1, 0.2, 1, 10\}\ \text{m s}^{-1}, \quad \mu_w = \{0.4, 0.5, 0.8, 1.2\},$$
$$h = (\mu_w/\mu_1 - 1)p_w/(\rho_* g \Phi) = [0.003, 0.911]\ \text{m},$$
$$\mathcal{A} = 0.108, \quad \mathcal{B} = 0.3744, \quad \mathcal{E} = 2.0957$$

Table 2. Definition of the parameters used to set the presented numerical simulations in this work. The numerical values for the size asymmetry coefficient χ_d (hence particle-size ratio R_d) and the frictional asymmetry coefficient χ_μ are used to set the particle parameters. The numerical values for pressure p_w, velocity u_w and frictional coefficient μ_w at the upper plate or wall (see figure 1) resulted in a range of values for h (see (2.4)) and set the granular rheology, together with the values of table 1. Finally, the empirical parameters $\mathcal{A}$, $\mathcal{B}$, $\mathcal{E}$ proposed by Trewhela *et al.* (2021*a*) and Utter & Behringer (2004) control the segregation dynamics in the numerical solutions.

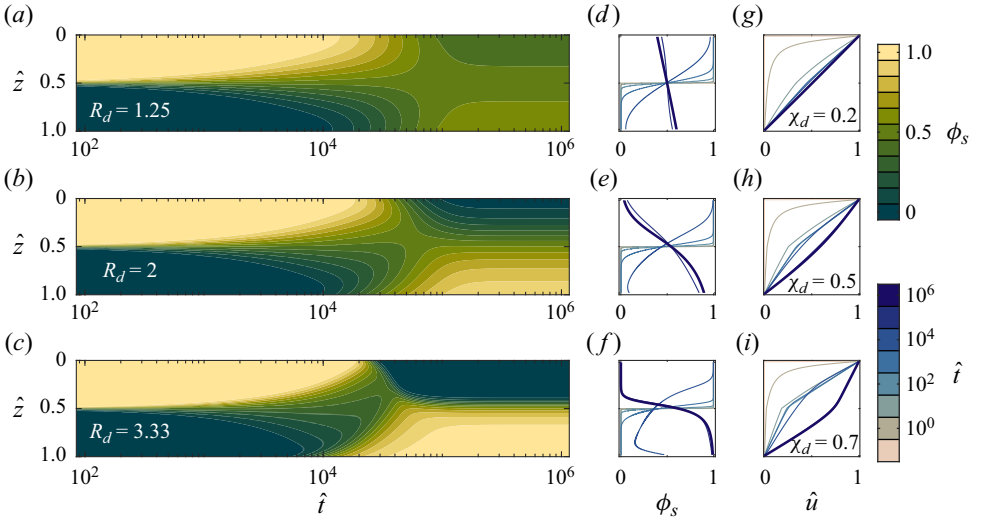

Figure 3. (*a–c*) Vertical and temporal distributions of small particle concentrations ϕ_s for $u_w = 0.2$ m s^{-1}, $p_w = 100$ Pa, $\mu_w = 0.5$ and $R_d = \{1.25, 2, 3.33\}$ values. (*d–f*) Small particle concentration profiles ϕ_s at different $\hat{t}$ times for the corresponding R_d values. (*g–i*) Velocity profiles $\hat{u}$ at different $\hat{t}$ instants for the corresponding R_d values, reflected in its asymmetrical coefficient $\chi_d = (R_d - 1)/R_d$ value. The thicker line in each of (*d–i*) highlights the final solution of each profile. Animated solutions of (*d–i*) are in supplementary movie 1, available at https://doi.org/10.1017/jfm.2024.168.

The asymmetric nature of segregation is captured clearly in figures 3(*a–c*). As the size ratio R_d increases, small particles segregate faster to the bottom compared to large particles arriving at the top. As a result, when asymmetry χ_d is increased, segregation fluxes are fast and dynamic, achieving the nonlinear steady-state swiftly (as observed for $R_d = 3.33$, $\chi_d = 0.7$ in figures 3*c*,*f*).

Other striking differences appear when comparing the final small particle concentrations ϕ_s. Larger R_d values produce sharper profiles with strongly segregated ϕ_s profiles and a marked small–large interface. Subsequently, this segregated and nonlinear distribution is imprinted into the shape of the steady-state velocity profile $\hat{u}$, thus a direct result of particle-size segregation effectiveness. For size ratios $R_d \to 1$, apparent mixing (i.e. diffusive remixing) is observed. Controlled by diffusion, mild segregation produces quasi-linear $\hat{u}$ profiles, as shown in figure 3(*d*). In contrast to these quasi-linear profiles, $\hat{u}$

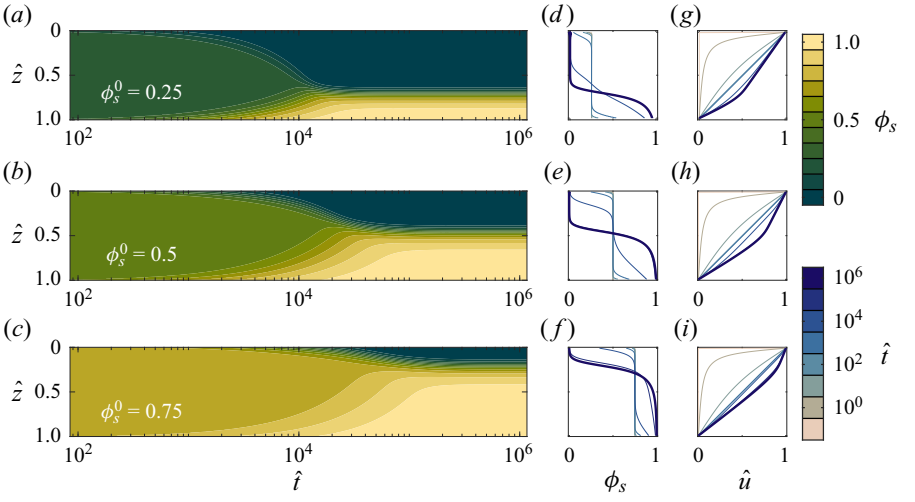

Figure 4. (*a–c*) Vertical and temporal distributions of small particle concentrations ϕ_s for $u_w = 0.2$ m s^{-1}, $p_w = 100$ Pa, $\mu_w = 0.5$ and $R_d = 3.33$ for initially-mixed conditions of small and large particles, $\phi_s^0 = \{0.25, 0.5, 0.75\}$. (*d–f*) Small particle concentration ϕ_s and (*g–i*) velocity $\hat{u}$ profiles at different $\hat{t}$ instants for the corresponding ϕ_s^0 and the same wall parameters and R_d value. The thicker line in each of (*d–i*) highlights the final solution of each profile. Animated solutions of (*d–i*) are available in supplementary movie 2.

solutions for large R_d show a sharp break in the velocity profile, drawing a rhomboid or lens geometry. The rhomboid is defined graphically by the linear responses expected for the normally graded and inversely graded conditions for particle-size distribution.

3.2. *Initially mixed conditions and resulting profiles*

The normally graded condition shown in figure 1(*a*) is a widely explored initial condition for segregation in experiments and numerical simulations (e.g. van der Vaart *et al.* 2015; Gray 2018; Chassagne *et al.* 2020). However, in the context of mixed bidisperse granular flows, the initially mixed condition illustrated in figure 1(*b*) also provides a valuable assessment on how segregation affects the rheology of granular mixtures. Figure 4 shows the resulting small particle concentration ϕ_s and velocity $\hat{u}$ profiles for three different initially mixed conditions of small and large particles at $\phi_s^0 = 25$, 50 and 75 % homogeneously mixed concentrations. To compare with the results shown previously in figures 3(*c*,*f*,*i*), an $R_d = 3.33$ value is used. The steady state ϕ_s distribution and the $\hat{u}$ profile observed in figures 4(*b*,*e*,*h*) are identical to those observed in figures 3(*c*,*f*,*i*). This agreement proves that steady-state solutions are independent of the normally graded or mixed initial conditions. Such independence is just about the particles' initial arrangement, and it is not extended to the average particle concentration ϕ_s^0, a condition that results in differing profiles for ϕ_s and $\hat{u}$ (figure 4).

As expected, there are important differences in the intermediate solutions for both ϕ_s and $\hat{u}$ due to the change in the initial conditions. Homogeneously mixed initial ϕ_s^0 concentrations produce not only different velocity $\hat{u}$ and skewed – but similar – ϕ_s profiles, but also delay segregation. The delayed steady-state solutions observed in figures 4(*a–c*) for larger ϕ_s^0 concentrations are tied inherently to the asymmetric nature of size segregation, i.e. the segregation flux $\boldsymbol{F}_s = f_{sl}\phi_s\phi_l\boldsymbol{g}/|\boldsymbol{g}| \sim (1 - \chi_d\phi_s)^2\phi_s(1 - \phi_s)$.

Small particles at low ϕ_s concentrations segregate at a faster rate than large particles at low ϕ_l concentrations (Gajjar & Gray 2014; van der Vaart *et al.* 2015; Trewhela *et al.* 2021*a*). If segregation fluxes were to be symmetric $\boldsymbol{F}_s = \phi_s\phi_l\boldsymbol{g}/|\boldsymbol{g}|$, then segregation rate would be maximum at $\phi_s^0 = 0.5$, and at identical rates for $\phi_s^0 = \{0.25, 0.75\}$ (Gray 2018). Therefore, figure 4 reproduce the expected asymmetry. For $\phi_s^0 = 0.25$, segregation alters the velocity profile solution swiftly from the mixed condition (at $\hat{t} \approx 10^2$) into the steady-state condition at almost $\hat{t} \approx 10^4$. In the case of $\phi_s^0 = 0.75$, segregation also initiates at $\hat{t} \approx 10^2$, but steady-state solutions are reached at a slower pace, i.e. at $\hat{t} \approx 10^5$. These differences hint at a ϕ_s-dependent time scale for segregation that controls the final duration of the segregation–rheology feedback.

3.3. *Influence of differences in the particles' frictional coefficients*

An additional effect in the Stokes' problem is explored by changing the small particles' frictional coefficient μ_s while keeping the size ratio $R_d = 2$ fixed, along with $p_w = 300$ Pa, $\mu_w = 0.5$ and $u_w = 0.2$ m s^{-1}. Differences in μ_s, relative to μ_l via R_μ, introduce a non-zero χ_μ value in (2.9*a*), which is null when small and large particles share the same $\mu(I)$-rheology parameters (table 1). Changes in χ_μ lead to velocity differences at the small–large particles interface, compromising the numerical scheme due to $\hat{u}$ discontinuity. Numerical solutions are found only for slight changes in χ_μ, within the interval $\chi_\mu = [-0.033, 0.013]$ for $R_d = 2$. This interval depends on the size ratio as well; as the size ratio R_d increases, the χ_μ interval for the solutions narrows.

In figure 5, ϕ_s and $\hat{u}$ solutions are plotted for various χ_μ values. While the small particle concentration ϕ_s solutions do not show significant differences between the different χ_μ cases, the velocity profiles $\hat{u}$ display interesting behaviour. For negative χ_μ values, μ_s is larger than μ_l, resulting in the transient solution having inverted slopes compared to the case with positive χ_μ values; see figures 5(*f*,*j*) for comparison. Intermediate negative values for χ_μ seem to counteract the $\hat{u}$ profile nonlinearity generated by the size difference in R_d (figures 5*g*,*h*). This finding is consistent with the proposed theoretical framework and could illustrate a way to obtain linear velocity profiles in granular flows with particles of varying sizes and frictional properties. Therefore, to control the particles' frictional properties is to partially control the segregation–rheology feedback, despite having a segregated bulk with different grain sizes.

3.4. *Steady-state analytical solutions and comparison with numerical solutions*

A solution for the transient velocity profiles $\hat{u}$ can be determined analytically from the steady-state condition in (2.9*a*), i.e. $\bar{\mu} = \mu_w$. This condition is replaced in the quadratic expression for I, obtained from the regularized $\mu(I)$-rheology in (2.2):

$$\mu_\infty I^2 + (\mu_2 - \mu_w)I + (\mu_1 - \mu_w)I_0 = 0. \tag{3.1}$$

The positive solution for I is then balanced with the inertial number I definition to yield a differential equation for the velocity $\hat{u}$. This ODE is solved by separating variables and using the no-slip boundary condition $\hat{u}|_{\hat{z}=1} = 0$ to yield

$$\hat{u} = \frac{h}{u_w \bar{d}}\sqrt{\frac{p_w}{\rho_*}}\,\mathcal{I}(\mu_w)\,(1 - \hat{z}), \tag{3.2}$$

where $\mathcal{I}(\mu_w) = ((\mu_w - \mu_2) + \sqrt{(\mu_w - \mu_2)^2 + 4\mu_\infty(\mu_w - \mu_1)I_0})/2\mu_\infty$ is the aforementioned positive solution of (3.1), i.e. the inertial number I. Equation (3.2)

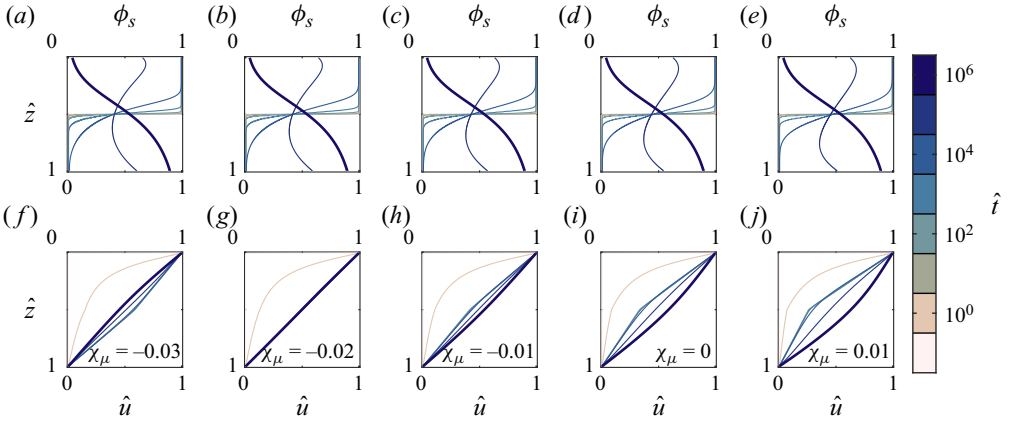

Figure 5. Numerical solutions for (*a–e*) small particle concentrations ϕ_s, and (*f–j*) velocity profiles $\hat{u}$ with constant wall parameters $u_w = 0.2$ m s^{-1}, $p_w = 300$ Pa, $\mu_w = 0.5$, $R_d = 2$, and variable $\chi_\mu = \{-0.03, -0.02, -0.01, 0, 0.01\}$ for (*a*,*f*), (*b*,*g*), (*c*,*h*), (*d*,*i*) and (*e*,*j*), respectively. The thicker line in each plot highlights the final solution of each variable. Solutions plotted in (*d*,*f–j*) are shown as animations in supplementary movie 3.

results in the rhomboid formation, already described and discussed in § 3.1. If the concentration-averaged diameter $\bar{d}$ is evaluated with the normally-graded size distribution, $\phi_s|_{\hat{z}=0}^{\hat{z}=1/2} = 1$ and $\phi_s|_{\hat{z}=1/2}^{\hat{z}=1} = 0$, and the inversely-graded size distribution, $\phi_s|_{\hat{z}=0}^{\hat{z}=1/2} = 0$ and $\phi_s|_{\hat{z}=1/2}^{\hat{z}=1} = 1$, then the rhomboid can be diagrammed. The solution captured by (3.2) provides a good approximation of the transient velocity profile without considering segregation in its development. When segregation determines the velocity profile, a steady-state solution for the small particle concentration ϕ_s can be obtained. For that, the procedure used by Trewhela *et al.* (2021*a*) is followed, yet their solution is implicit for ϕ_s. Here, a simpler differential equation is developed from $\mathcal{E} = 0$ (a first-order approximation in $R_d - 1$), resulting in the explicit solution

$$\phi_s = \frac{\mathrm{e}^{(\hat{z}+\mathcal{K})/\lambda}}{1 + \mathrm{e}^{(\hat{z}+\mathcal{K})/\lambda}}, \tag{3.3}$$

where $\mathcal{K} = -1/2$ is the constant of integration, which can be calculated using the depth-averaged condition $\bar{\phi}_s = \int_0^1 \phi_s \,\mathrm{d}\hat{z} = 0.5$, and $\lambda = \mathcal{A}p_w/(\mathcal{B}\rho g h(R_d - 1))$. This small particle concentration ϕ_s profile serves as input for the generalized ODE:

$$\frac{\mathrm{d}\hat{u}}{\mathrm{d}\hat{z}} = -\frac{h}{u_w \bar{d}}\sqrt{\frac{p_w}{\rho_*}}\,\mathcal{I}(\hat{\mu}_w), \tag{3.4}$$

where $\hat{\mu}_w = \mu_w(1 - 2.7(1 - \phi_s)\chi_\mu)/(1 - \chi_\mu\phi_s)$ is a ϕ_s- and χ_μ-dependent frictional coefficient, with $\bar{d}$ a function of the former as well. Due to this dependence, the ODE's solution is computed using a Runge–Kutta fourth-order method.

Figure 6 summarizes the core behaviour of the segregation–rheology feedback. The transient-state solution of (3.2) and its reciprocal stable state (red and blue toned rhomboids) are shown in figure 6(*a*). These rhomboids emphasize the slope change in $\hat{u}$ as R_d increases, with the fully linear case $R_d = 1$ as reference. In figure 6(*b*), the generalized solution in (3.4) is drawn for the $R_d = 2$ case and various χ_μ values, with the reference

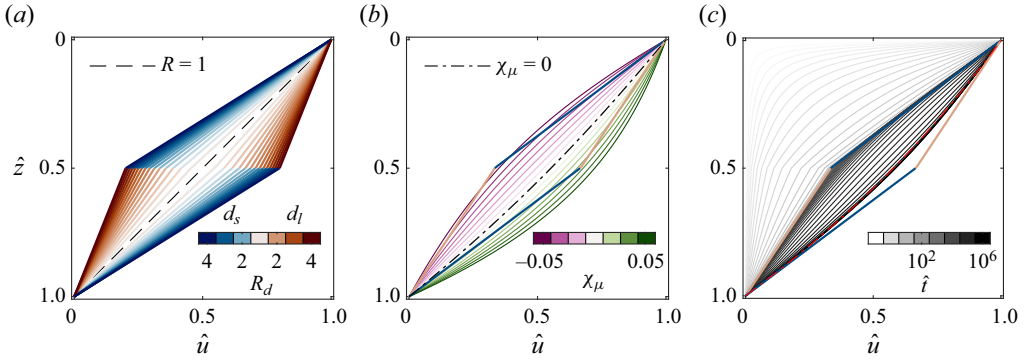

Figure 6. (*a*) Velocity profiles $\hat{u}$ for the steady-state condition in (3.2) for various $R_d = [1, 4]$ values, represented in blue and red tones for d_s and d_l, respectively. (*b*) Velocity profiles $\hat{u}$ of the numerically solved (3.4) for variable $\chi_\mu = [-0.05, 0.05]$ and constant $R_d = 2$, with its corresponding rhomboid from (*a*). (*c*) Temporal evolution of the velocity profile $\hat{u}$ for the $R_d = 2$ and $\chi_\mu = 0.01$ case compared with the corresponding steady-state solutions from (*a*) ((3.2), plotted as a rhomboid) and (*b*) ((3.4), plotted with a dot-dashed line). Note how the velocity profiles $\hat{u}$ first collapse around the rhomboid solution, and then converge to the steady-state solution (red dot-dashed line). Fully animated solutions (for $\chi_\mu = \{-0.03, -0.01, 0.01\}$ and constant $R_d = 2$), compared to the steady-state solutions of (3.2) and (3.4), are shown in supplementary movies 4–6.

curve $\chi_\mu = 0$ at the middle. Negative χ_μ values tend to displace the steady-state velocity profile $\hat{u}$ towards the linear reference, acting as a counterpart for the deviation generated by the size ratio R_d. Conversely, positive χ_μ values exacerbate the nonlinear behaviour of the velocity profiles $\hat{u}$, displacing the curves beyond the reciprocal stable-state curve (with large particles over small ones). Moreover, solutions attempting to pass beyond the stable state could explain the difficulties in obtaining solutions when the frictional asymmetric coefficient is $\chi_\mu > 0.013$ for $R_d = 2$. A detailed evolution of the velocity profile $\hat{u}$ solutions is shown in figure 6(*c*). The velocity profile $\hat{u}$ develops from the initial condition to the transient state $\hat{t} \sim 10^2$, adjusting well to the analytical solution of (3.2) (left rhomboid linear curves in figure 6(*c*), taken from $R_d = 2$ in figures 6*a*,*b*). Then segregation alters this state, rearranging particles according to their size, achieving a steady state at $\hat{t} \approx 10^5$ that fits well the ODE solution in (3.4) (dot-dashed line in figure 6*c*). In figure 6(*c*) the segregation–rheology feedback ends up being described graphically by the changes in $\hat{u}$ from the transient to the steady state, hence analytically bounded within the R_d-dependent rhomboid region.

3.5. *Granular kinematic viscosity, time scales and segregation–momentum balances*

From the ODE for the non-dimensional shear rate $\hat{\dot{\gamma}} = |\mathrm{d}\hat{u}/\mathrm{d}\hat{z}|$ in (3.4), a general definition for the granular kinematic viscosity ν_g can be formulated. Using the theoretical constitutive relation for a granular dynamic viscosity $\tau = \mu p = \eta_g \dot{\gamma}$ (Jing *et al.* 2022), the dimensional kinematic viscosity can be defined as

$$\nu_g = \frac{\hat{\mu}_w \bar{d}}{\mathcal{I}(\hat{\mu}_w)} \sqrt{\frac{p_w}{\rho_*}}. \tag{3.5}$$

Compared to the granular viscosity definition of Jerome & Di Pierro (2018), in (3.5) this bidisperse granular viscosity is R_d-, χ_μ- and ϕ_s-dependent (via $\bar{d}$ and $\hat{\mu}_w$), and is still determined by the wall conditions and the $\mu(I)$-rheology parameters (table 1). It is worth

recalling that the $\mathcal{I}$ function is in fact the inertial number I, but for the Stokes' problem analysed in this work, it is left as the function defined in (3.2).

The definition of ν_g allows the analysis of the different time scales at which the segregation–rheology feedback develops. Evidently, a first time scale appears from the non-dimensional time $\hat{t}$ definition, where $t_{\dot{\gamma}} \sim h/u_w$ can be defined as a convective or shear rate time scale, inferred from $1/\dot{\gamma} = (\mathrm{d}u/\mathrm{d}z)^{-1} \approx h/u_w$ (as in the definition of I; GDR-MiDi 2004). A second time scale can be associated with momentum diffusing through the granular bulk and derived directly from (3.5), yielding

$$t_{\nu_g} \sim \frac{h^2}{\nu_g} = \frac{h^2\,\mathcal{I}(\hat{\mu}_w)}{\hat{\mu}_w \bar{d}} \sqrt{\frac{\rho_*}{p_w}}. \tag{3.6}$$

Then two more time scales appear from the particle-segregation-related processes. A segregation time scale is drawn by the time it takes particles of diameter $\bar{d}$ to segregate through the sheared layer h with velocity f_{sl}:

$$t_{f_{sl}} \sim \frac{h}{f_{sl}} = n_{\bar{d}} P\,\mathcal{F}(R_d, \phi_s)^{-1}\, t_{\dot{\gamma}}, \tag{3.7}$$

where $n_{\bar{d}} = h/\bar{d}$ is the number of particle layers through the sheared layer depth, $\mathcal{F}(R_d, \phi_s) = \mathcal{B}(R_d - 1)[1 + \mathcal{E}(R_d - 1)(1 - \phi_s)]$ is a function defined from the segregation velocity f_{sl} function, and $P = p_w/(\rho_* g \bar{d})$ corresponds to a non-dimensional pressure (Trewhela *et al.* 2021*a*). The segregation time scale is proportional to $t_{\dot{\gamma}}$ and p_w, in agreement with the clear segregation dependence on shear rate and pressure (Golick & Daniels 2009; Trewhela *et al.* 2021*b*). Thus the segregation time scale $t_{f_{sl}}$ is the shear rate time scale $t_{\dot{\gamma}}$ modulated by pressure conditions at the wall, segregation, and the number of layers that particles must segregate through. Finally, the particle diffusion time scale can be defined as

$$t_{\mathcal{D}_{sl}} \sim \frac{h^2}{\mathcal{D}_{sl}} = \frac{n_{\bar{d}}^2}{\mathcal{A}}\, t_{\dot{\gamma}}, \tag{3.8}$$

which again is proportional to $t_{\dot{\gamma}}$. Although these time scales do not provide the actual time that the velocity $\hat{u}$ and small particle concentration ϕ_s profiles take to reach their corresponding steady-state solutions, which is out of the scope of this work, they serve to describe the progression of the segregation–rheology feedback.

For the numerical solutions computed in § 3.1, $t_{\dot{\gamma}} = 0.0157$ s and the momentum diffusion time scale share similar values $t_{\nu_g} \approx 0.15$ s, yielding a non-dimensional time $\hat{t} = t_{\nu_g}/t_{\dot{\gamma}} \approx 10$ for the $\hat{u}$ profiles to develop into the transient solution. This value is close to what is shown in figure 3, with $\hat{t} \approx 10^2$ being the time at which the transient solution is achieved in the computations. In terms of segregation, there are larger differences in $t_{f_{sl}} \approx \{100, 20, 7\}$ s and $t_{\mathcal{D}_{sl}} = \{80, 120, 170\}$ s for $R_d = \{1.25, 2, 3.33\}$, respectively. These $t_{f_{sl}}$ values capture well the faster set in of segregation at $\hat{t} = t_{f_{sl}}/t_{\dot{\gamma}} \approx \{6 \times 10^3, 10^3, 5 \times 10^2\}$ for the same R_d values. However, these $t_{f_{sl}}$ are balanced out by shorter or larger diffusive time scales $t_{\mathcal{D}_{sl}}$, which finally settle the concentration profiles into their steady-state solution. Consistent results are observed when analysing these time scales in the case of the initially mixed condition solutions at fixed $R_d = 3.33$. These yield the same $t_{\dot{\gamma}}$ and t_{ν_g} values for all solutions, but $t_{f_{sl}} \approx \{3, 7, 20\}$ s and $t_{\mathcal{D}_{sl}} \approx \{100, 170, 310\}$ s increase with $\phi_s^0 = \{0.25, 0.5, 0.75\}$, resulting in the monotonic increase

of $\hat{t} = t_{\mathcal{D}_{sl}}/t_{\dot{\gamma}} \approx \{7 \times 10^3, 10^4, 2 \times 10^4\}$. These values are also similar to the times found in the numerical solutions (figure 4). In the case of the varying χ_μ solutions, there are only slight differences in t_{ν_g}. Values decrease from approximately 0.9 s to 0.7 s as χ_μ goes from -0.03 to 0.01.

From these results and the analysed time scales, it is thus natural to compare the two diffusion processes acting in the bidisperse granular Stokes' problem. With the definition of the granular momentum diffusivity time scale, or its diffusivity coefficient in ν_g, the Schmidt number or the ratio of the momentum and particle diffusivity time scales is obtained directly as

$$Sc = \frac{t_{\nu_g}}{t_{\mathcal{D}_{sl}}} = \frac{\nu_g}{\mathcal{D}_{sl}} = \frac{\hat{\mu}_w}{\mathcal{A} I^2}, \tag{3.9}$$

where the inertial number is reintroduced for simplicity and generalization; for that matter, I can be considered equal to $d\dot{\gamma}/\sqrt{p/\rho_*}$ or equal to the definition of $\mathcal{I}$ made after (3.2). It is worth noting that the I^2 term corresponds to the Savage or Coulomb number (Savage 1984; Ancey, Coussot & Evesque 2000). Low Sc values indicate an important particle diffusivity (diffusive remixing), dominating over momentum diffusion, which at first glance can be achieved with low μ_w, high $\mathcal{A}$ or high inertial numbers I. Conversely, a large Sc points towards a more viscous response from the granular material, with a lesser role played by particle diffusion in the overall flow dynamics. Interestingly, this definition of the Schmidt number depends implicitly not only on the particles' concentration-averaged diameter $\bar{d}$ (via I), hence their size ratio R_d and size asymmetry coefficient, but also on the frictional asymmetry coefficient χ_μ and the particles' frictional parameters.

To illustrate these dependencies, figure 7(*a*) shows the Schmidt number Sc as a function of both μ_w and an overall small particle concentration, which can be interpreted as the initial small particle concentration ϕ_s^0 or the depth-averaged small particle concentration $\overline{\phi_s} = \int_0^1 \phi_s \, \mathrm{d}\hat{z}$. In figure 7(*a*), the contours' slope is determined by χ_μ: positive χ_μ yields a negative slope (dashed contours), and vice versa (filled contours). For the computed values in the domain $\mu_w = [0.4, 1.2]$ and $\phi_s = [0, 1]$, Sc varies from 10^3 to 10^{-1}, decreasing linearly in two regions marked approximately by $\mu_w \lessgtr \mu_2 = 0.557$. This is a direct result of the partially regularized $\mu(I)$-rheology, which allows $\mu_w > \mu_2$, therefore extending the range for Sc. Overall, Sc decreases with μ_w, and increases slightly with higher ϕ_s^0, when $\chi_\mu < 0$. The former observation contradicts the linear dependence of Sc on μ_w, but is consistent with the fact that high μ_w values result in high I values as well, since $Sc \sim I^{-2}$. (For more results shedding light on the role of μ_w, see Appendix A.) While particle diffusivity scales with the shear rate $\mathcal{D}_{sl} \sim \dot{\gamma}$ (Utter & Behringer 2004), the granular viscosity scales inversely with the latter $\nu_g \sim \dot{\gamma}^{-1}$; so larger friction at the wall produce high shear rates and will result in low Sc. But as stated before, the segregation–rheology feedback is not a purely momentum- or particle-diffusion-dominated process; segregation also controls the flow dynamics.

To understand better at which extent segregation controls the segregation–rheology feedback, a particle segregation–diffusion balance is borrowed from previous work. Following the definitions made by Gray (2018) and Trewhela *et al.* (2021*a*), a Péclet number for segregation Pe can be defined as the ratio between the segregation velocity f_{sl} and particles' diffusivity $\mathcal{D}_{sl}$, i.e. $Pe = hf_{sl}/\mathcal{D}_{sl}$, or alternatively, $t_{f_{sl}}/t_{\mathcal{D}_{sl}}$. With this definition, a specific Péclet number for the segregation–rheology feedback can be

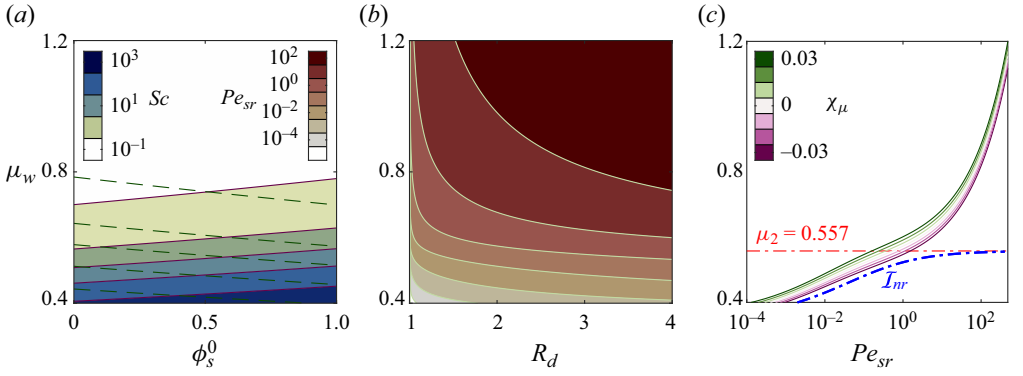

Figure 7. (*a*) Filled contours for the Schmidt number $Sc = t_{\nu_g}/t_{\mathcal{D}_{sl}} = \nu_g/\mathcal{D}_{sl}$ as a function of both μ_w and the overall small particle concentration ϕ_s^0, in the case $\chi_\mu = -0.03$. Dashed contours show the change of slope in the case $\chi_\mu = 0.03$ for the same Sc values of the filled contours. (*b*) Filled contours for the segregation–rheology Péclet number $Pe_{sr} = t_{f_{sl}}/t_{\nu_g} = hf_{sl}/\nu_g$ as a function of μ_w and the size ratio R_d, in the case $\chi_\mu = 0.01$. (*c*) Variation of the segregation–rheology Péclet number Pe_{sr} as a function of the wall friction μ_w and the frictional asymmetry parameter χ_μ. For comparison, the constant frictional parameter $\mu_2 = 0.557$ is plotted alongside the same Pe_{sr}, but using the non-regularized inertial number definition $\mathcal{I}_{nr} = I_0(\mu_w - \mu_1)/(\mu_2 - \mu_w)$, which is independent of χ_μ (dot-dashed thick line).

introduced as

$$Pe_{sr} = \frac{Pe}{Sc} = \frac{hf_{sl}}{\nu_g} = \frac{t_{f_{sl}}}{t_{\nu_g}} = \frac{I^2}{\Phi_p \hat{\mu}_w}\,\mathcal{F}(R_d, \phi_s), \tag{3.10}$$

where $\Phi_p = p_w/(\rho g h)$ is a non-dimensional pressure, which can be interpreted as an equivalent solids volume fraction. Again, this second non-dimensional quantity depends on I^2 (or the Savage number). Compared to the previous Sc definition, the segregation–rheology Péclet number Pe_{sr} depends on the size ratio R_d and the empirical constants determined by Trewhela *et al.* (2021*a*). The proposed Pe_{sr} somehow confirms the results discussed previously in §§ 3.1 and 3.3, where segregation profiles were sharper for large R_d (figure 3) and positive χ_μ values (figure 5).

Figures 7(*b*,*c*) show the variation of the segregation–rheology Péclet number Pe_{sr} as a function of $\hat{\mu}_w$, μ_w and R_d. Broadly, the Pe_{sr} dependence on R_d is well captured in figure 7(*b*). As expected, Pe_{sr} is minimum for $R_d \to 1$, and interestingly, larger size differences do not necessarily result in predominant segregation effects over momentum diffusion, since $Pe_{sr} = 0.01$ for $R_d = 4$ and $\mu_w = 0.4$. Therefore, the results presented in the previous subsections are summarized conceptually in the Pe_{sr} definition; the segregation–rheology feedback is relevant when a combination of both high friction and large size differences is in place. Nonetheless, high μ_w is still enough to promote segregation, even accompanied by low R_d. All this, as long as there is sufficient pressure p_w or the bulk is compressed (Φ_p) enough at the wall to transfer shear without restraining both momentum and segregation. The latter opens the possibility of including compressibility effects in the proposed system and solutions. In figure 7(*c*), the Pe_{sr} curves are plotted for various χ_μ values, all of which show similar behaviour. However, when Pe_{sr} is calculated using the non-regularized $\mu(I)$-rheology, i.e. $\mathcal{I}_{nr} = I_0(\mu_w - \mu_1)/(\mu_1 - \mu_w)$, the Pe_{sr} value diverges as $\mu_w \to \mu_2$ (thick dashed line in figure 7*c*). This shows the importance of having a well-posed extended formulation for the $\mu(I)$-rheology. When using the partially regularized $\mu(I)$-rheology, Pe_{sr} continues to increase monotonically with $\mu_w > \mu_2$, but at a lower rate than for $\mu_w < \mu_2$, and without a clear cutoff value.

4. Conclusions

The segregation–rheology feedback in dense granular flows was explored numerically and theoretically via Stokes' first problem for a bidisperse granular bulk at constant solids volume fraction. Using this paradigmatic problem for such a nonlinear and coupled system required the implementation of the method of lines, which proved to be a practical numerical scheme despite the issues inherited from the $\mu(I)$-rheology implementation. The solved PDE system incorporated the partially regularized $\mu(I)$-rheology of Barker & Gray (2017) and the scaling law for bidisperse size segregation of Trewhela *et al.* (2021*a*). The results focused on the role of size ratio R_d in the development of velocity profiles, and included the effect of frictional differences or a frictional ratio R_μ between particle species via the introduced parameter $\chi_\mu = (R_\mu - 1)/R_\mu$, in analogy with the segregation asymmetry coefficient $\chi_d = (R_d - 1)/R_d$. Under a constant pressure p_w condition, the numerical solutions showed a transient state, decoupled from the segregation process, achieving linear velocity profiles $\hat{u}$. Then segregation-induced feedback alters particle concentrations, thus changing the linear $\hat{u}$ state into a ϕ_s- and R_d-dependent nonlinear solution for $\hat{u}$. The transient and steady-state solutions encompass a rhomboid region that expands as R_d increases, and reduces to a single linear profile when $R_d \to 1$ (with no segregation). The steady-state solution is determined not only by R_d but also by the particles' frictional coefficient ratio R_μ. While positive χ_μ values exacerbate the solutions' nonlinearity, negative values of χ_d dampen the effect of R_d and favour a linear behaviour, counteracting the segregation-induced feedback. The numerical solutions converge well around the analytical expressions (3.2) and (3.4), which bound the feedback's solution range.

The kinematic granular viscosity ν_g was redefined based on the partially regularized $\mu(I)$-rheology and the concentration-averaged diameter $\bar{d}$, hence determined locally by particle concentrations ϕ_v. Four characteristic time scales arising from shear rate $t_{\dot{\gamma}}$, granular momentum diffusion t_{ν_g}, segregation $t_{f_{sl}}$ and particle diffusion $t_{\mathcal{D}_{sl}}$ were introduced to describe the progression of the segregation–rheology feedback. These time scales did not provide precise expressions for the time at which the variables attained the transient and steady states, but explained well the observed temporal differences in the presented numerical results. From ν_g and these four time scales, two non-dimensional numbers appeared naturally as a result of segregation–momentum balances: a Schmidt number $Sc = \nu_g/\mathcal{D}_{sl}$, and a specific segregation–rheology Péclet number $Pe_{sr} = hf_{sl}/\nu_g$. These two quantities not only showed consistency with the numerical and theoretical results, but also provided a broad description for the segregation–rheology feedback and its dependence on the plethora of parameters addressed here.

Although the coupled Stokes' problem is an idealized case study, the developed analyses provide a robust numerical scheme for particle-size segregation in granular flows that is easy to compare with experimental results and applicable to the rheometry of dense granular flows (e.g. Golick & Daniels 2009; Trewhela & Ancey 2021). Particle-size segregation and local friction redistribution, as discussed in this work, may have consequences for the scales associated with shear bands (May *et al.* 2010), or other processes like jamming (Rietz & Stannarius 2008). Further research is required to extend this feedback analysis towards an extended range of size ratios and flow characteristics – compressibility, reverse segregation or other segregation mechanisms – that are still not considered but could complement or fit well in the presented approach (Schaeffer *et al.* 2019; Neveu *et al.* 2022).

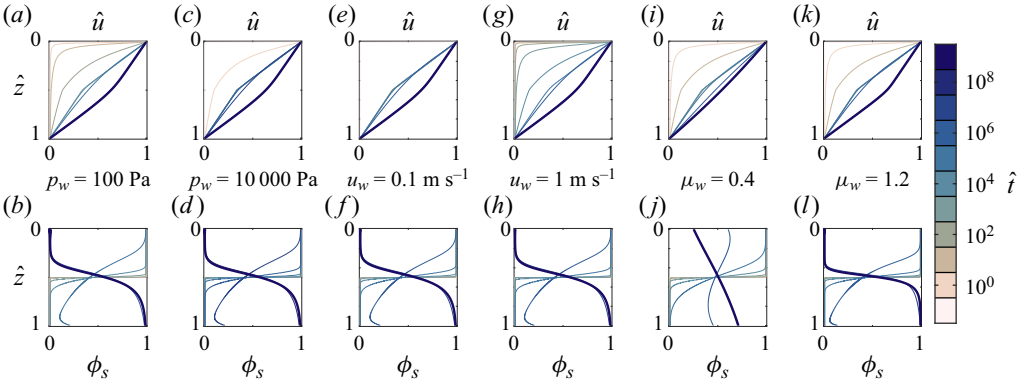

Figure 8. Influence of wall parameters in small particle concentrations ϕ_s (top row) and velocity profiles $\hat{u}$ (bottom row) for: (*a–d*) variable wall pressure $p_w = \{100, 10\,000\}$ Pa and constant wall velocity $u_w = 1$ m s^{-1} and frictional coefficient $\mu_w = 0.8$; (*e–h*) variable wall velocity $u_w = \{0.1, 10\}$ m s^{-1} and constant wall pressure $p_w = 1000$ Pa and frictional coefficient $\mu_w = 0.8$; and (*i–l*) variable wall frictional coefficient $\mu_w = \{0.4, 1.2\}$ and constant wall pressure $p_w = 1000$ Pa and velocity $u_w = 1$ m s^{-1}. In these solutions, $\chi_d = 0$, with the empirical parameters in tables 1 and 2. The thicker line in each plot highlights the final profile of each variable.

Supplementary movies. Supplementary movies are available at https://doi.org/10.1017/jfm.2024.168.

Acknowledgements. The author thanks J. Dumais, J.M.N.T. Gray, L. Gordillo and H. Ulloa for their constructive comments on this paper. The colour maps used in this paper are readable by both colour-vision-deficient and colour-blind people (Crameri 2018).

Funding. This research received support from Agencia Nacional de Investigación y Desarrollo (ANID) through FONDECYT Iniciación Project 11240630, Dirección de Investigación of Universidad Adolfo Ibañez through Programa de Apoyo a la Investigación, and Facultad de Ingeniería y Ciencias through their Startup Package.

Declaration of interests. The author reports no conflict of interest.

Author ORCIDs.
Tomás Trewhela https://orcid.org/0000-0002-7461-8570.

Appendix A. Role of wall parameters p_w, u_w and μ_w

The segregation–rheology feedback is dominated primarily by the particles' size ratio R_d and the frictional asymmetry coefficient χ_μ. The pressure p_w, velocity u_w and frictional coefficient μ_w at the wall also influence and control both the segregation and rheology, through shear and pressure, hence the inertial number I. Roughly, in the numerical solutions, the combination of these three wall parameters tunes the rate at which momentum is transferred into the bulk. To address the role of each of these parameters, a set of solutions is obtained for variable p_w, u_w and μ_w values while keeping the rest of the parameters constant, including R_d and χ_μ, which were set to 2 and 0, respectively. Figure 8 shows the results of varying these parameters, and the effect they have on the resulting profiles for the explored Stokes' problem. The results can be separated into three subsets of solutions, one for each varying parameter.

A direct comparison between figures 8(*a*,*b*) and 8(*c*,*d*) indicates that larger p_w values enhance the transfer of momentum, while restraining segregation, hence stretching the duration of the segregation–rheology feedback. Some of these observations made for p_w are inverted in the case of u_w. In the case $u_w = 0.1$ m s^{-1} in figure 8(*e*), the transient $\hat{u}$

profile is achieved swiftly with the resulting shear rate $\dot{\gamma}$. Yet this has little effect on the segregation velocity. Since $f_{sl} \sim \dot{\gamma}$, segregation takes longer for low $\dot{\gamma}$, hence delaying the segregation–rheology feedback, as observed in figure 8(f). Conversely, as figure 8(g) shows, larger u_w values take longer times to diffuse through the bulk, but once shear is well transferred, segregation comes along fast. The associated time scales $t_{\dot{\gamma}} \sim h/u_w$ for the large $p_w = 10\,000$ Pa case is equal to that case where $u_w = 0.1$ m s^{-1}, i.e. $t_{\dot{\gamma}} = 0.9101$ s. This result is derived from the height h dependence on p_w. It is worth noting that all the resulting ϕ_s and $\hat{u}$ profiles for the mentioned cases are the same, with changes observed only in the associated time scales for the momentum and segregation transfer processes and their feedback.

When μ_w is changed, the resulting ϕ_s and $\hat{u}$ profiles change accordingly. A decrease in $\mu_w = 0.4$ towards $\mu_1 = 0.342$ results in a diffused ϕ_s profile (see figure 8j), which translates into a linear response in $\hat{u}$, as shown in figure 8(i). We have the opposite case for $\mu_w = 1.2$, which produces a sharply segregated ϕ_s profile with its corresponding rhomboid solution for $\hat{u}$. This observation emphasizes the role of friction on the segregation–rheology feedback and is a result of the nonlinear and local dependence of both processes on the $\mu(I)$-rheology.

References

Ancey, C., Coussot, P. & Evesque, P. 2000 A theoretical framework for granular suspensions in a steady simple shear flow. *J. Rheol.* **43** (6), 1673–1699.

Ancey, C. & Evesque, P. 2000 Frictional-collisional regime for granular suspension flows down an inclined channel. *Phys. Rev.* E **62** (6), 8349–8360.

Bancroft, R.S.J. & Johnson, C.G. 2021 Drag, diffusion and segregation in inertial granular flows. *J. Fluid Mech.* **924**, A3.

Barker, T. & Gray, J.M.N.T. 2017 Partial regularisation of the incompressible $\mu(I)$-rheology for granular flow. *J. Fluid Mech.* **828**, 5–32.

Barker, T., Rauter, M., Maguire, E., Johnson, C. & Gray, J.M.N.T. 2017 Coupling rheology and segregation in granular flows. *J. Fluid Mech.* **909**, A22.

Cawthorn, C.J. 2011 Several applications of a model for dense granular flows. PhD thesis, University of Cambridge.

Chassagne, R., Maurin, R., Chauchat, J., Gray, J.M.N.T. & Frey, P. 2020 Discrete and continuum modelling of grain size segregation during bedload transport. *J. Fluid Mech.* **895**, A30.

Crameri, F. 2018 Scientific Colour Maps. Zenodo. Available at: http://doi.org/10.5281/zenodo.1243862.

Delannay, R., Valance, A., Mangeney, A., Roche, O. & Richard, P. 2017 Granular and particle-laden flows: from laboratory experiments to field observations. *J. Phys.* D*: Appl. Phys.* **50**, 053001.

Denissen, I.F.C., Weinhart, T., Te Voortwis, A., Luding, S., Gray, J.M.N.T. & Thornton, A.R. 2019 Bulbous head formation in bidisperse shallow granular flow over an inclined plane. *J. Fluid Mech.* **866**, 263–297.

Edwards, A.N., Rocha, F.M., Kokelaar, B.P., Johnson, C.G. & Gray, J.M.N.T. 2023 Particle-size segregation in self-channelized granular flows. *J. Fluid Mech.* **955**, A38.

Gajjar, P. & Gray, J.M.N.T. 2014 Asymmetric flux models for particle-size segregation in granular avalanches. *J. Fluid Mech.* **757**, 297–329.

GDR-MiDi 2004 On dense granular flows. *Eur. Phys. J.* E **14** (4), 341–365.

Golick, L.A. & Daniels, K.E. 2009 Mixing and segregation rates in sheared granular materials. *Phys. Rev.* E **80** (4), 042301.

Gray, J.M.N.T. 2018 Particle segregation in dense granular flows. *Annu. Rev. Fluid Mech.* **50**, 407–433.

Guillard, F., Forterre, Y. & Pouliquen, O. 2016 Scaling laws for segregation forces in dense sheared granular flows. *J. Fluid Mech.* **807**, R1.

Henann, D.L. & Kamrin, K. 2013 A predictive, size-dependent continuum model for dense granular flows. *Proc. Natl Acad. Sci.* **110**, 6730–6735.

Holyoake, A.J. & McElwaine, J.N. 2012 High-speed granular chute flows. *J. Fluid Mech.* **710**, 35–71.

Jerome, J.J.S. & Di Pierro, B. 2018 A note on Stokes' problem in dense granular media using the $\mu(I)$-rheology. *J. Fluid Mech.* **847**, 365–385.

JING, L., OTTINO, J.M., UMBANHOWAR, P.B. & LUEPTOW, R.M. 2022 Drag force in granular shear flows: regimes, scaling laws and implications for segregation. *J. Fluid Mech.* **948**, A24.

JONES, R.P., ISNER, A.B., XIAO, H., OTTINO, J.M., UMBANHOWAR, P.B. & LUEPTOW, R.M. 2018 Asymmetric concentration dependence of segregation fluxes in granular flows. *Phys. Rev. Fluids* **3** (9), 094304.

JOP, P., FORTERRE, Y. & POULIQUEN, O. 2006 A constitutive relation for dense granular flows. *Nature* **44**, 727–730.

JORDAN, P.M. & PURI, A. 2005 Revisiting Stokes' first problem for Maxwell fluids. *Q. J. Mech. Appl. Maths* **58** (2), 213–227.

KAMRIN, K. & KOVAL, G. 2012 Nonlocal constitutive relation for steady granular flow. *Phys. Rev. Lett.* **108**, 178301.

KIM, S. & KAMRIN, K. 2020 Power-law scaling in granular rheology across flow geometries. *Phys. Rev. Lett.* **125**, 088002.

LARCHER, M. & JENKINS, J.T. 2019 The influence of granular segregation on gravity-driven particle–fluid flows. *Adv. Water Res.* **129**, 365–372.

MAY, L.B.H., GOLICK, L.A., PHILLIPS, K.C., SHEARER, M. & DANIELS, K.E. 2010 Shear-driven size segregation of granular materials: modeling and experiment. *Phys. Rev.* E **81**, 051301.

MIDDLETON, G.V. 1970 Experimental studies related to problems of flysch sedimentation. In *Flysch Sedimentology in North America* (ed. J. Lajoie), pp. 253–272. Business and Economics Science Ltd.

NEVEU, A., LARCHER, M., DELANNAY, R., JENKINS, J.T. & VALANCE, A. 2022 Particle segregation in inclined high-speed granular flows. *J. Fluid Mech.* **935**, A41.

PREZIOSI, L. & JOSEPH, D.D. 1987 Stokes' first problem for viscoelastic fluids. *J. Non-Newtonian Fluid Mech.* **25** (3), 239–259.

RAYLEIGH, LORD 1911 On the motion of solid bodies through viscous liquid. *Phil. Mag.* **6** (82), 697–711.

RIETZ, F. & STANNARIUS, R. 2008 On the brink of jamming: granular convection in densely filled containers. *Phys. Rev. Lett.* **100**, 078002.

ROGNON, P.G., ROUX, J.N., NAAÏM, M. & CHEVOIR, F. 2007 Dense flows of bidisperse assemblies of disks down an inclined plane. *Phys. Fluids* **19** (5), 058101.

SAVAGE, S.B. 1984 The mechanics of rapid granular flows. *Adv. Appl. Mech.* **24**, 289–366.

SAVAGE, S.B. & LUN, C.K.K. 1988 Particle size segregation in inclined chute flow of dry cohesionless granular solids. *J. Fluid Mech.* **189**, 311–335.

SCHAEFFER, D.G., BARKER, T., TSUJI, D., GREMAUD, P., SHEARER, M. & GRAY, J.M.N.T. 2019 Constitutive relations for compressible granular flow in the inertial regime. *J. Fluid Mech.* **874**, 926–951.

SCHIESSER, W.E. & GRIFFITHS, G.W. 2009 *A Compendium of Partial Differential Equation Models: Method of Lines Analysis with Matlab*. Cambridge University Press.

STEWARTSON, K. 1951 On the impulsive motion of a flat plate in a viscous fluid. *Q. J. Mech. Appl. Maths* **4** (2), 182–198.

STOKES, G.G. 1850 On the effect of the internal friction of fluids on the motion of pendulums. *Trans. Camb. Phil. Soc.* **9** (8), 1.

TOKUDA, N. 1968 On the impulsive motion of a flat plate in a viscous fluid. *J. Fluid Mech.* **33**, 657–672.

TREWHELA, T. & ANCEY, C. 2021 A conveyor belt experimental setup to study the internal dynamics of granular avalanches. *Exp. Fluids* **62**, 207.

TREWHELA, T., ANCEY, C. & GRAY, J.M.N.T. 2021*a* An experimental scaling law for particle-size segregation in dense granular flows. *J. Fluid Mech.* **916**, A55.

TREWHELA, T., GRAY, J.M.N.T. & ANCEY, C. 2021*b* Large particle segregation in two-dimensional sheared granular flows. *Phys. Rev. Fluids* **6**, 054302.

TRIPATHI, A. & KHAKHAR, D.V. 2011 Rheology of binary granular mixtures in the dense flow regime. *Phys. Fluids* **23** (11), 113302.

UMBANHOWAR, P.B., LUEPTOW, R.M. & OTTINO, J.M. 2019 Modeling segregation in granular flows. *Annu. Rev. Chem. Biomol. Engng* **10**, 129–153.

UTTER, B. & BEHRINGER, R.P. 2004 Self-diffusion in dense granular shear flows. *Phys. Rev.* E **69**, 031308.

VAN DER VAART, K., GAJJAR, P., EPELY-CHAUVIN, G., ANDREINI, N., GRAY, J.M.N.T. & ANCEY, C. 2015 Underlying asymmetry within particle size segregation. *Phys. Rev. Lett.* **114**, 238001.

VAN DER VAART, K., THORNTON, A.R., JOHNSON, C.G., WEINHART, T., JING, L., GAJJAR, P., GRAY, J.M.N.T. & ANCEY, C. 2018 Breaking size-segregation waves and mobility feedback in dense granular avalanches. *Granul. Matt.* **20**, 46.

WOODHOUSE, M.J., THORNTON, A.R., JOHNSON, C.G., KOKELAAR, B.P. & GRAY, J.M.N.T. 2012 Segregation-induced fingering instabilities in granular free-surface flows. *J. Fluid Mech.* **709**, 543–580.